High frequency glow discharges at atmospheric pressure with micro-structured electrode arrays

L Baars-Hibbe[1], P Sichler[2], C Schrader[1], N Lucas[2], K-H Gericke[1] and S Büttgenbach[2]

[1] Institut für Physikalische and Theoretische Chemie, Technische Universität Braunschweig, Hans-Sommer-Straße 10, D-38106 Braunschweig, Germany
[2] Institut für Mikrotechnik, Technische Universität Braunschweig, Alte Salzdahlumer Str. 203, D-38124 Braunschweig, Germany

Abstract
Micro-structured electrode (MSE) arrays allow the generation of large-area uniform glow discharges over a wide pressure range up to atmospheric pressure. The electrode widths, thicknesses and distances in the micrometre range are realized by means of modern micro-machining and galvanic techniques. The electrode distance, the gap width d, is small enough to generate sufficiently high electric field strengths to ignite gas discharges by applying only moderate radio frequency (RF, 13.56 MHz) voltages (80–390 V in Ne, He, Ar, N_2 and air). The non-thermal plasma system is characterized by a special probe measuring the electric parameters. We tested MSE arrays with $d = 70$, 25 and 15 μm. The MSE driven plasmas show a different behaviour from conventional RF discharge plasmas. Due to the very small electrode gap width we can describe the behaviour of the charged particles in the RF field of our system with the dc Townsend breakdown theory, depending on the pressure range and gas. With decreasing pressure, the gas discharges, especially in Ne and He, are increasingly dominated by field electron emission. With the MSE arrays as plasma sources several applications were developed and successfully tested, e.g. decomposition of waste gases and sterilization of food packaging materials at atmospheric pressure.

1. Introduction

There is growing interest in non-thermal plasma processing techniques optimized for atmospheric pressure applications due to their significant industrial advantages. At atmospheric pressure, thin film deposition at very high rates is possible, and cost-intensive vacuum technology can be avoided. Many approaches have been proposed in the last 15 years to overcome the problems of generating and sustaining a stable, uniform and homogeneous non-thermal atmospheric pressure plasma. Massines *et al* [1, 2], Okazaki *et al* [3, 4], Trunec *et al* [5] and Roth *et al* [6–8] successfully generated atmospheric pressure glow discharges with a dielectric barrier array, and Selwyn and co-workers [9, 10] developed a radio frequency (RF) atmospheric pressure plasma jet producing a stable and homogeneous plasma.

There are two approaches based on the Paschen similarity law (pd = const.), which scale down the electrode dimensions in the micrometre range in order to ignite discharges at atmospheric pressure, at moderate voltages, working in the Paschen minima of the different gases. Schoenbach *et al* [11, 12], Schmidt-Böcking and co-workers [13] and Eden *et al* [14, 15] use a micro-hollow-cathode-array in order to generate atmospheric pressure glow discharges. Recently, we and our project partners introduced micro-structured electrode (MSE) arrays, consisting of a system of planar and parallel electrodes (comb structure), as alternative atmospheric pressure plasma sources [16–20]. The electrodes (see figure 1) are arranged on an insulating substrate and manufactured by means of modern micro-machining and galvanic techniques. The electrode dimensions, especially the electrode gap width d in the micrometre range, are small enough to generate sufficiently

high electric field strengths to ignite atmospheric pressure glow discharges applying only moderate (RF, 13.56 MHz) voltages (less than 400 V). The same design is used for surface barrier discharges, where the comb structure is embedded into the dielectric barrier structure [21]. With this last type of plasma source a plasma can be generated in air at atmospheric pressure, but not as a homogeneous glow discharge, in contrast to the MSE generated plasmas.

In this publication, we characterize the ignition parameters of the MSE-driven RF plasmas for the electrode gap widths 25 and 15 μm and compare it with the results of the 70 μm MSE array already published [22, 23]. The parameters show a special behaviour, which differs from conventional RF and dc discharges. After breakdown the RF plasmas are characterized in the operational range used by the applications. Several successful applications are reviewed, e.g. decomposition of waste gases and sterilization of food packaging materials.

2. Fabrication of micro-structured electrode arrays

Figure 1 shows an MSE array and the electrode gap design for gap widths $d = 25$ and 15 μm. The design and fabrication of MSE arrays with $d = 70$ μm, already published in [20], was modified for the gap widths $d = 25$ and 15 μm in order to guarantee the same actual gap shape for all three samples. All three MSE samples have an electrode width of 1350 μm and an electrode length of 7200 μm. The electrode thickness is varied with d in order to reduce deviations of the gap shape and distance (see below) due to the influence of sidewall slopes: the 70 μm electrodes are 100 μm thick, the 25 μm electrodes are 35 μm thick and the 15 μm electrodes are 25 μm thick.

Although the plasmas generated are of non-thermal type, only thermally rugged materials can be used for micro-structured electrodes. Therefore, nickel is electroplated on an alumina substrate. Alumina substrates are commonly used in thick film technology. In contrast to this technology, micro-structures with high aspect ratios (ratio of height to width) of up to 5 or 10 have to be achieved. While most photolithographic processes focus on submicrometre resolutions on fine polished silicon wafers with reflective or absorbing properties [24], in this case, a dispersive surface is given. A roughness R_a of 6.5 μm is measured with a Tencor P10 profiler on a scan length of 1 mm. This is due to the sintering of ceramics and cannot
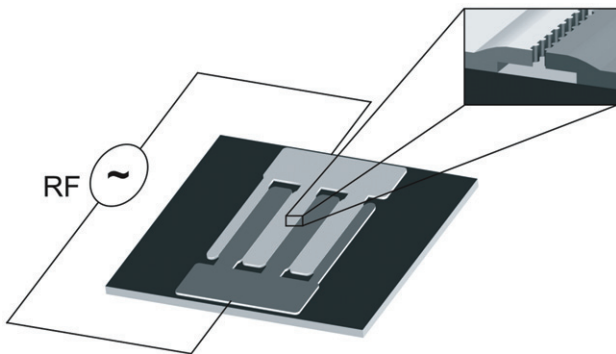
be eliminated sufficiently by grinding. Experiments have shown that dispersive effects dominate the resulting sidewalls of photoresists with decreasing gap width, starting at 25 μm.

Therefore, a smooth, nondispersive wafer surface is necessary. This is achieved by sputter coating a cleaned alumina wafer with copper and subsequent spin coating of a 20 μm thick SU8 (Micro Chem) layer (see figure 2(a)). Measurements indicate a roughness R_a of 0.1 μm for the SU8 surface (Tencor P10, scan length 150 μm). After drying, the SU8 is exposed through a mask to UV radiation creating the acids necessary for cross linking [25]. In this step the copper layer serves as an optical absorption layer for the SU8 lithography. The cross linking is accomplished on a hotplate at 95°C after 45 min. Development of the SU8 layer is done in γ-butyrolactone (GBL) and propylene glycol methyl ether acetate (PGMEA) (figure 2(b)) in a beaker with manual agitation. Residuals of resin on the rough alumina surface are removed with a short descum in a CF$_4$–O$_2$-plasma (80 sccm O$_2$, 20 sccm CF$_4$, 100 W, 4 min). The copper layer is now removed in Alketch (Candor Chemie). After 1 h of dehydration at 120°C a second copper layer is sputtered on the sample. It serves as the seed layer for electrodeposition and is subsequently covered with AZ 9260 (Clariant) resist as shown in figure 2(c). This resist is spun on twice at 600 rpm with 1 h of drying on a hotplate after each spin step. Conditioning has to be performed for 10 h before the exposure to UV-light through a chromium mask, at a dose of 2400 mJ cm^{-2}. The sample is developed and plated with nickel in a sulphamate-type bath with additives for reduction
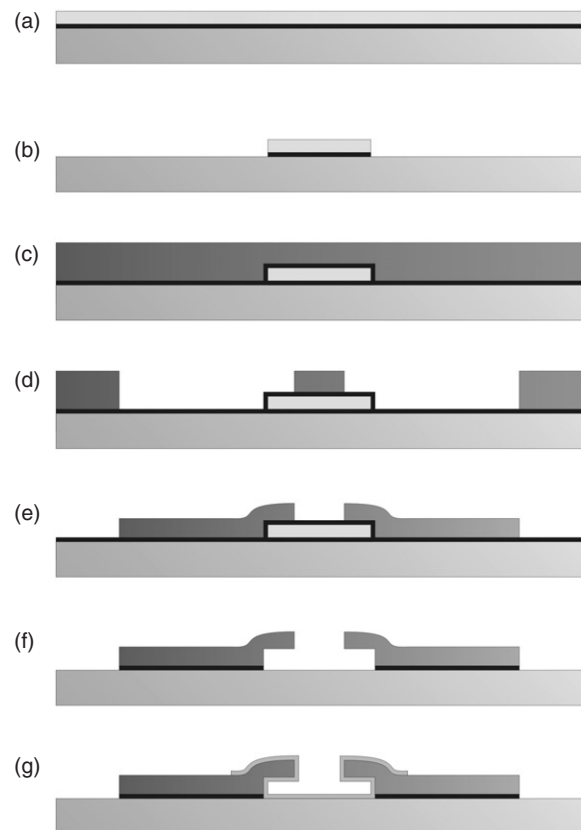

Figure 1. Schematic view of an MSE array with the electrode gap design shown in detail.

Figure 2. Production sequence of the micro-structured electrode (MSE) arrays.

of residual stress. At $15 \, mA \, cm^{-2}$ for 2 h a thickness of $30 \, \mu m$ is achieved with sufficient uniformity to avoid subsequent grinding. After stripping the AZ 9260 resist (figure 2(*e*)) the second copper layer is etched as described above. The SU8 is ashed in an intense CF_4–O_2-plasma (80 sccm O_2, 20 sccm CF_4, 300 W, 30 min). By etching the first copper layer the remaining electric shortcut between the electrodes is removed (figure 2(*f*)). Finally, a $0.5 \, \mu m$ thick alumina layer is sputter deposited all over the electrodes (figure 2(*g*)). The necessary free space on top of the pads can be achieved by using a shadow mask in the sputter process.

3. Experimental

The experimental set-up is schematically shown in figure 3. The MSE arrays were installed into a complex vacuum system providing a virtually laminar gas flow with a rate of 200 sccm set up by means of mass flow controllers. The gas inlet system and vacuum system are described in detail in [19]. The discharges were generated using an RF (13.56 MHz) power supply (ENI ACG-3B) equipped with an impedance matching network (ENI MW-5D). The RF generator is power controlled from 0 to 300 W in steps of 1 W. The generator power P_{gen} used for measurements and applications ranged between 3 W (ignition) and 35 W in Ne, 5 and 40 W in He, and between 18 and 45 W in N_2, depending on the pressure or application. A special probe (ENI VI-Probe) was inserted between the matching network and the MSE array in order to measure voltage U, current I, phase angle φ and effective power P_{eff} of the system. The effective powers input into the plasma were dependent on the chosen gas and generator power, but independent of pressure (range from 10 to 100 kPa). A chromel–alumel thermocouple of K-type was placed directly under the substrate of the MSE array to measure the temperature rise of the MSE array during plasma operation.
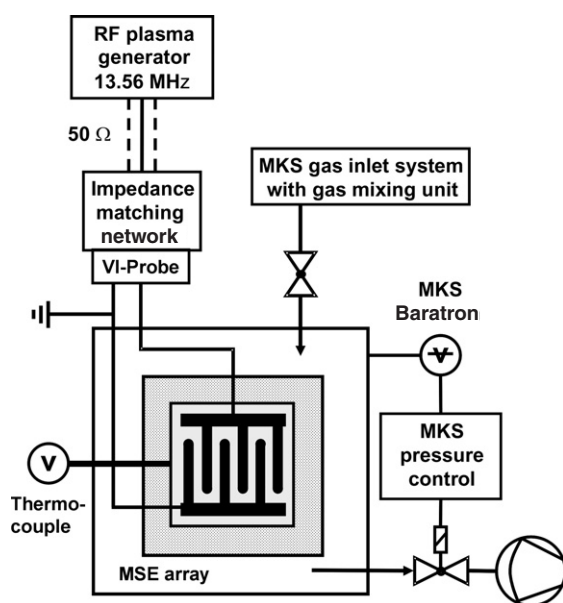
4. Characterization of the MSE plasma

The electrode gap has a complex geometry with incorporated protrusions (see figure 1) allowing the generation of large-area uniform glow discharges in He and Ne at pressures up to 150 kPa and in Ar and N_2 up to 120 kPa [20]. With the 25 and $15 \, \mu m$ structures glow discharges can be generated even in air up to 50 kPa. The discharges are non-thermal [19, 20] and generated at the five gaps between the electrodes. In the gases Ne, He and Ar the plasma covers all electrode gaps; in N_2 at a pressure higher than 60 kPa the plasma covers only one electrode gap. Up to a pressure of 40 kPa the plasma covers the whole electrode system (see figure 1), and in N_2 a high applied generator power (>45 W) is necessary to do so. The maximum measured temperature rises of the MSE array are 395 K in He and 420 K in N_2. Analogous to the effective power, the temperature rise is dependent on the applied generator power, but independent of pressure (range from 10 to 100 kPa).

Figure 4 shows the voltage–current characteristic of a 40 kPa N_2 RF plasma generated with an MSE array ($d = 70 \, \mu m$). The curve progression is characteristic for a glow discharge and is very similar to the characteristic of a low pressure dc discharge [26]. The voltage–current characteristics of N_2 with $d = 25$ and $15 \, \mu m$ as well as the characteristics of He and Ne are very similar to the N_2 characteristic presented up to a pressure of 100 kPa. The operational range is the normal glow range including the subnormal glow range showing the characteristic hysteresis behaviour. The abnormal glow is only obtained in 10 kPa N_2 with a high applied generator power. At too high applied generator powers, the electrodes of the MSE arrays start to age with increasing occurrence of sparks over time (especially in N_2 and air).

The characterization of the ignition parameters of the RF plasmas generated by the $70 \, \mu m$ MSE arrays has previously been published [22, 23]. Due to the very small electrode gap width we can describe the behaviour of the charged particles in the RF field of our system with the dc Townsend breakdown theory, depending on the pressure range and gas type.

In order to explain the observed behaviour figure 5 shows the oscillation amplitudes z_0 of the charged particles calculated

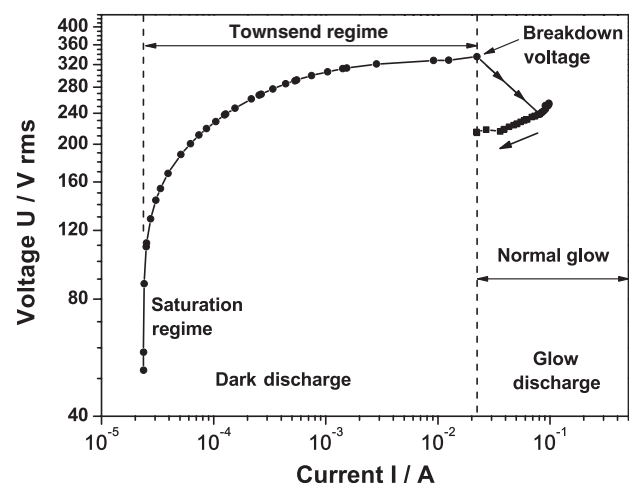
Figure 3. Schematic of the experimental set-up. The gas inlet system and vacuum system are published in detail in [19].

Figure 4. Voltage–current characteristic of a 40 kPa N_2 RF glow discharge with an MSE array ($d = 70 \, \mu m$).

with the measured electric field strength E using equation (1):

$$z_0 = \frac{e E_0}{m\omega\sqrt{\omega^2 + \nu_c^2}},$$ (1)

where E_0 is the field amplitude, m the mass of the charged particle, ω the angular frequency ($2\pi \times 13.56$ MHz) and ν_c the e^-–neutral collision frequency. This equation gives the extreme values derived from the solution (2) of the equation of motion, including the pressure dependent Lorentz collisional term in order to account for friction [26]:

$$z = -\frac{e E_0 \nu_c}{m\omega(\omega^2 + \nu_c^2)} \cos(\omega t) - \frac{e E_0}{m(\omega^2 + \nu_c^2)} \sin(\omega t).$$ (2)

The motion of the charged particles is drift controlled analogously to dc discharges, because the amplitudes of the electrons as well as the ions exceed $d/2$ (35 μm) [27], with the exception of Ne at pressures higher than 80 kPa (see figure 5). With $d = 25$ and 15 μm the amplitudes z_0 of all gases not only exceed $d/2$ (12.5 and 7.5 μm) but also d in the entire pressure range of 10–100 kPa. Thus, the dc Townsend breakdown mechanism must be the dominating breakdown mechanism. Figures 6–8 show the experimental breakdown voltages (ignition potentials U_{IP}) of the gases N_2, He and Ne with $d = 70$, 25 and 15 μm. Where the experimental curves resemble the Paschen curves, they are fitted with the Paschen formula [28, 29] derived from the dc Townsend breakdown theory:

$$U_{IP} = \frac{B \cdot (p \cdot d)}{C + \ln(p \cdot d)}$$ (3)

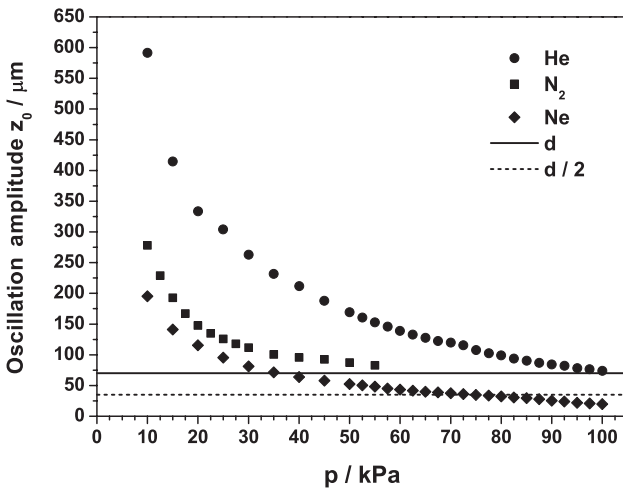**Figure 5.** Ion oscillation amplitudes for $d = 70\,\mu$m calculated with the measured electric field strengths.

with

$$C = \ln \frac{A}{\ln((1/\gamma) + 1)}.$$ (4)

The fitted constants B and C are listed in table 1. The B values of the RF experiment determined for $d = 70\,\mu$m are lower than the B values of the dc field [28], because the voltages required to initiate and maintain ac discharges decrease strongly in comparison to dc glow discharges with increasing frequency [29]. Thus, there is always a contribution of the high frequency discharge regime to the breakdown mechanism. With $d = 25$ and 15 μm the B values of N_2 correspond to the dc values and the dc Townsend breakdown mechanism is dominant.

Figure 6 compares the dc breakdown voltages in N_2 [28] with the experimental RF breakdown voltages for different values of d. The standard deviation is omitted for better clarity. The standard deviation describes the margin of deviation between three manufactured MSE samples and varies in figure 6 between 3% and 12%. The B value of the 70 μm Paschen curve is only slightly lower than the dc value and the dc Townsend breakdown mechanism dominates the ignition with a small contribution of the high frequency discharge regime. With the decrease of d to 25 μm the breakdown voltage is lowered. The small increase of B cannot explain this effect, which should rather result in an increase of the breakdown voltage. Since with all d the dc Townsend breakdown mechanism is dominant, we can estimate with the tabulated constant A the experimental secondary electron emission coefficient γ. In table 2 the estimated experimental γ values of all gases calculated with equation (4) are summarized and compared with dc γ and γ_i (electron emission by ion bombardment of the cathode) values. A higher contribution of γ_i to the ignition (with $d = 25\,\mu$m) can be excluded, since the calculated ion kinetic energies of N_2 have almost identical values at the same pd values for both electrode distances. With $d = 25\,\mu$m the estimated γ value even exceeds the dc value. Hartherz [30] have shown that with d values in the micrometre range the breakdown voltages are increasingly dominated by field electron emission with decreasing pressure, although the electric field strengths used are below 10^6 V cm^{-1} [28] characteristic for dc experiments. Thus, a strong increase of the contribution of field electron emission is responsible for this effect, because the ignition electric field strengths are more than doubled. In N_2, the additional decreasing of d to 15 μm results only in a small additional decrease in the breakdown voltage, confirmed by a small increase of γ.

The B value of Ne is more than one magnitude smaller than the dc value, which can only partly be explained by the non-matching regions of applicability. In the entire fitted pressure range, at pressures above 80 kPa, the ion oscillation

Table 1. Fitted constants of the Paschen formula for three different electrode gap widths d and regions of applicability (B and E/p in V kPa^{-1} cm^{-1}).

		Experiment (RF)			Literature [28] (dc)	
d (μm)	Gas	B	C	E_{eff}/p	B	E/p
70	Ne	67.2 ± 4.3	0.92 ± 0.03	110–200	750	750–3000
70	He	157.3 ± 2.3	1.28 ± 0.01	170–280	260	150–1000
70	N_2	2378 ± 52	3.28 ± 0.04	1020–2820	2560	750–4500
25	N_2	2611 ± 67	3.51 ± 0.03	1490–3140	2560	750–4500
15	N_2	2611 ± 87	3.52 ± 0.03	2000–4890	2560	750–4500

amplitudes of Ne do not exceed $d/2$ (see figure 5). Thus, the breakdown controlling regime is a mixture of the high frequency discharge mechanism [27, 29] and the dc Townsend breakdown mechanism, where the high frequency mechanism is dominant. In He neither of both breakdown regimes is dominant. However, the contribution of the dc Townsend breakdown mechanism is higher than in Ne, because all amplitudes z_0 of He exceed $d/2$. With increasing pressure, the ion oscillation amplitudes z_0 decrease and, consequently, the high frequency discharge mechanism becomes more dominant. The estimated experimental γ values of both gases confirm this interpretation—they are much lower than the dc values.

As already published [22, 23], at low pressures (below 40 kPa) in He and Ne the dc breakdown mechanism is dominant. With all three electrode gap widths d the breakdown voltages are identical for a certain gas and pressure. At the breakdown, the whole surface of the electrodes is covered with a darker diffuse plasma compared to the intense plasma generated only at the gaps between the electrodes at high pressures. Thus, higher breakdown distances are favoured to the shortest electrode gap width d. The MSE driven discharges of Ne and He at pressures lower than 40 kPa represent the left-hand branches of the Paschen curves (see figure 7) near the minimum, with higher effective d values (see [23] for details).

Analogous to Ne, in Ar with $d = 70\,\mu$m a transition occurs from the dc Townsend breakdown mechanism at low pressure to the high frequency discharge mechanism at atmospheric pressure (see [23] for more details). With $d = 25$ and $15\,\mu$m
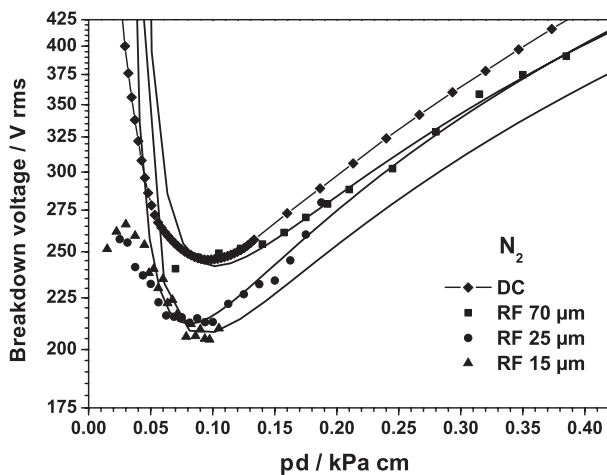

Figure 6. Fitted Paschen curves in N_2. Comparison of the dc breakdown voltages [28] with the experimental RF breakdown voltages for different values of d. The standard deviation is omitted for better clarity.

analogous to N_2, the dc Townsend breakdown mechanism is dominant.

While the Paschen curves for He and Ne ($d = 70\,\mu$m) fit the experimental data very well at high pd values, they deviate significantly at lower pd values (see figure 7). Between 40 and 80 kPa the breakdown voltage is independent of pressure. Theoretically, much higher breakdown voltages are expected due to the growing lack of impact partners with decreasing pd values. As mentioned above, with d in the micrometre range, field electron emission contributes to the breakdown mechanism, which is also independent of pressure. Thus, with $d = 70\,\mu$m in He and Ne field electron emission dominates the breakdown mechanism in the pressure range between 40 and 80 kPa [22, 23]. With $d = 25$ and $15\,\mu$m the field electron emission dominates the breakdown mechanism at pressures above 40 kPa. Due to the smaller d values the electric field strengths are much higher than with $d = 70\,\mu$m and a significant additional lowering of the breakdown voltages is expected with a higher contribution of the field electron emission. The experimentally observed lowering of the breakdown voltages with the reduction of d to $15\,\mu$m is about 5% in He and Ne. For comparison, the lowering of the breakdown voltages in N_2 is about 12% due to much higher electric breakdown field strengths. The breakdown mechanism is always a mixture of field electron emission, the dc Townsend breakdown regime and the high frequency discharge regime: the field electron emission dominates the breakdown mechanism, but does not cause an additional significant lowering of the breakdown voltages with decreasing d. Hartherz *et al* [30] observed in air (breakdown voltages normally above 300 V) only with d smaller than $10\,\mu$m at 10 kPa and $4\,\mu$m at 100 kPa a significant lowering of the breakdown voltages with decreasing d. Under these conditions the field electron emission entirely controls the breakdown mechanism. Figure 8 shows the experimental breakdown voltages with $d = 15\,\mu$m in Ne, He, Ar, N_2 and air as well as the fitted Paschen curves in Ar and N_2. In air, there are not enough reproducible data points for a good fit. With the shortest distance $d = 15\,\mu$m, analogous to Ne and He, the field electron emission dominates the breakdown mechanism in Ar at pressures lower than 40 kPa and in N_2 at pressures lower than 25 kPa. This behavior is an advantage of the micro-structured electrode arrays, because the breakdown voltage is lowered.

If we compare the RF breakdown voltages in He and Ne with the breakdown voltages of conventional dc discharges (see figure 7), we can see that the RF breakdown voltages are much lower than the dc breakdown voltages, which cannot be explained only by the lowering effects of the high frequency regime and field electron emission. Particularly, if we compare He and Ne with N_2, there must be an additional effect lowering

Table 2. Estimated experimental secondary electron emission coefficients γ calculated using equation (4).

d (μm)	Gas	A (kPa^{-1} cm^{-1}) Literature [28]	C Experiment (RF)	γ	γ_i (E_{kin} range) Literature [31] (dc)
70	Ne	30.0	0.92 ± 0.03	6.63×10^{-6}	0.12–0.14 (5–90 eV)
70	He	22.5	1.28 ± 0.01	1.95×10^{-3}	ca. 0.17 (5–90 eV)
70	N_2	90.0	3.28 ± 0.04	3.53×10^{-2}	4.4×10^{-2}[a]
25	N_2	90.0	3.51 ± 0.03	7.33×10^{-2}	4.4×10^{-2}[a]
15	N_2	90.0	3.52 ± 0.03	7.55×10^{-2}	4.4×10^{-2}[a]

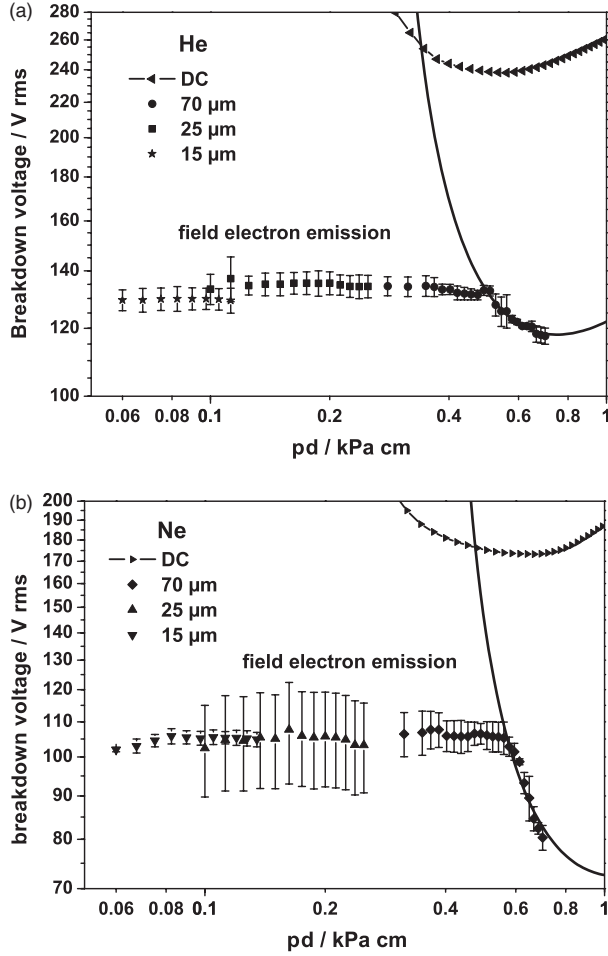[a] γ calculated from literature data [28].

Figure 7. Fitted Paschen curves in He and Ne. Comparison of the dc breakdown voltages [28] with the experimental RF breakdown voltages for different values of d. The standard deviation describes the margin of deviation between three manufactured MSE samples.
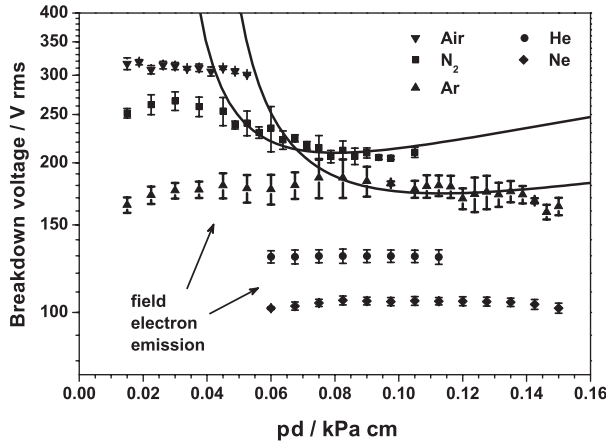

Figure 8. Experimental breakdown voltages and fitted Paschen curves in Ne, He, Ar, N_2 and air ($d = 15 \, \mu m$, 10–100 kPa). The standard deviation describes the margin of deviation between three manufactured MSE samples.

the breakdown voltages. The reason is the main difference between ac (RF) and dc: for ac the voltage passes through a sinusoidal curve with the two extreme values $\pm U_0$ and two nodes during each period, whereas for dc the voltage is

constant. The ionization energies of Ne (21.6 eV) and He (24.6 eV) are significantly higher than the ionization energy of N_2 (15.6 eV). Additionally, N_2 is a molecule with rotational and vibrational states. These states of N_2 can be excited by electron impact excitation with electron energies lower than the ionization energy of N_2. These excitations cause an additional loss of electron kinetic energy missing for the ionization process of the ignition mechanism. The lowest excited states of Ne ($^3P_2$, 16.6 eV) or He ($^3S_1$, 19.8 eV) possess energies, which are still higher than the ionization energy of N_2. Therefore, electrons with kinetic energies lower than 16.6 eV and 19.8 eV, respectively, cannot excite Ne or He in contrast to N_2; the electrons can accumulate more energy up to the ionization level. Thus, the loss of energy in the ionization process is much lower than in N_2. This makes the difference between ac and dc: the measured RF breakdown voltages U_{IP} are effective voltages (rms values): the voltages periodically increase to a value of

$$U_0 = \sqrt{2} \cdot U_{IP} \qquad (5)$$

and decrease to values near 0 V. Voltages higher than U_{IP} provide a much higher ionization probability for the gases Ne and He. Concurrently, voltages significantly lower than U_{IP} are not high enough to excite Ne or He. The electrons accelerated in an electric field with a strength of $E < E_{IP}$ (ignition field strength) are still able to excite the rotational and vibrational states of N_2. In N_2 this additional electron energy loss compensates the ac advantage of $E > E_{IP}$; only in Ne and He a significant lowering of the breakdown voltage is observed. This theoretical interpretation is confirmed by optical emission spectroscopy [32].

As already published [23], we estimate the electron density n_e of the RF glow discharge with a simple model used by Park *et al* [10], where n_e is calculated using equation (6):

$$\frac{I_p}{A_p} = -n_e \cdot e \cdot \mu_e \cdot E \qquad (6)$$

with the measured plasma current I_p (see figure 4), the active plasma area A_p and the electron mobility $\mu_e = 0.0424 \, m^2 \, V^{-1} \, s^{-1}$ for N_2 [33]. The electric field strength E is an effective field strength [23] lowered by the factor ε, the measured and pressure dependent dielectric constant of the medium. The electron density in He at a pressure of 100 kPa is 2.3×10^{17} electrons per m^3 [23], which is high, but still characteristic for a glow discharge [26]. The estimated electron densities in N_2 at the pressures 10 and 40 kPa are somewhat higher than in He, because in N_2 with $P_{gen} = 25$ W only two of five electrode gaps are covered with plasma. Thus, the N_2 active plasma area is only $\frac{2}{5}$ of the He active plasma area. With n_e we can estimate the Debye shielding distance λ_D calculated with equation (7) [26, 29, 34]

$$\lambda_D = \sqrt{\frac{\varepsilon_0 \cdot k \cdot T_e}{e^2 \cdot n_e}} \qquad (7)$$

in order to get some information about the sheath thickness, where ε_0 is the permittivity of vacuum, k the Boltzmann constant and T_e the electron temperature. The MSE plasma source generates electrons with kinetic energies of more than 20 eV

Table 3. The estimated Debye length λ_D in N_2 for the pressures 10 and 40 kPa ($d = 70\,\mu m$, $P_{gen} = 25\,W$, $P_{eff} = 7.4\,W$).

p (kPa)	λ (μm)	ε	n_e (m^{-3})	Degree of ionization x	T_e (eV)	λ_D (μm)
10	0.957	1.146	3.23×10^{17}	1.33×10^{-7}	1	13
					5	29
					20	58
40	0.239	1.035	1.31×10^{18}	1.35×10^{-7}	1	7
					5	15
					20	29

[19]. It is not possible to measure an electron energy distribution function with a conventional Langmuir probe due to the small dimensions of the system [23]. Thus, in table 3 we summarized the results for three different T_e in each case. λ_D is more than one magnitude higher than the mean free path length λ and of the same magnitude as the width of the bulk plasma and the electrode gap width $d = 70\,\mu m$. These ratios are very different from those for conventional dc or RF systems.

In order to discuss the role of λ_D in stabilizing the plasma against sparking or the influence of λ_D on other effects we have to carry out more experiments, especially in N_2 and air. Currently, we are carrying out new experiments with $d = 25$ and $15\,\mu m$ in order to develop a new model for our system, which is very interesting, because in this case there is a theoretical possibility of λ_D being greater than d.

5. Applications

In He and N_2 the decomposition of the greenhouse gas CF_4 was performed with rates of over 90% at a pressure of 10 kPa with the MSE array as a plasma source incorporated into a micro-reactor. At atmospheric pressure the abatement rate in He is still over 70% [20, 35]. Additionally, the abatement of NO in 100 kPa He has been investigated [30, 36], where a decomposition rate of 70% is achieved.

Another application is the sterilization and deposition set-up (see [22] for details) consisting of the MSE plasma source coplanarly arranged above a substrate (Si, Cu or different plastic films). The MSE plasma source releases and accelerates electrons generating fluorescent excited atoms and ions. These species are the sterilizing agents for the thermo-resistant spores of the vegetative bacteria *Bacillus cereus* and the UV-resistant spores of the fungus *Aspergillus niger* at atmospheric pressure in He and Ar [22]. This is proved by optical emission spectroscopy [32]: below 300 nm (UV-range for sterilizing the spores) no emission lines could be detected. The substrate is biased with various potentials (up to 1500 Vpp) in order to accelerate the reactive plasma species towards the substrate. With this set-up we successfully deposited diamond-like carbon layers or SiO_2 layers on various substrates (Si, Cu, polymer films) with a deposition rate of 30 nm min^{-1} (9.5 kHz ac bias up to 1000 Vpp) [17, 20, 22].

6. Summary and conclusions

With the MSE array we have an alternative atmospheric pressure plasma source with many applications: plasma chemistry (decomposition of waste gases like CF_4), thin film deposition (e.g. SiO_2 layers on various substrates) and sterilization of food packaging materials.

The MSE driven radio frequency glow discharges show a special ignition behaviour, which differs from that of conventional high frequency and dc gas discharges. Due to the very small electrode gap width (15–70 μm) we can describe the behaviour of the charged particles in the RF field of our system with the dc Townsend breakdown theory, depending on the pressure range and gas type. With increasing pressure, the contribution of the high frequency discharge mechanism rises until it dominates the breakdown mechanism. On the other hand, with decreasing pressure and reduction of the electrode gap width, the gas discharges, especially in Ne and He, are increasingly dominated by field electron emission, which is an advantage of the micro-structured electrode systems, because the breakdown voltage is lowered.

With the dc behaviour, especially shown by the discharges in N_2 and air, two disadvantageous effects are observed: sputtering of the electrode material and the necessity to decouple the single electrode fingers in order that all electrode gaps are covered with plasma. One method of decoupling the electrode fingers is to integrate resistors on the MSE arrays, which complicates the manufacturing process. First experiments were successful with this new type of MSE array: in N_2 all electrode gaps were at least partially covered with plasma, which improved the power and heat distribution at high pressures and slowed down the ageing process.

The better option is to increase the radio frequency. With very high frequencies (more than 100 MHz) the high frequency regime should dominate the breakdown mechanism, even in air and with a very small electrode distance (less than 10 μm), which is favourable due to the high contribution of field electron emission. Both solutions (very high frequency coupled with $d < 10\,\mu m$) simultaneously result in lower breakdown voltages at high pressures and slow down the ageing of the MSE arrays, because the disadvantage of a dc discharge—sputtering—is completely avoided.

References

[1] Massines F, Rabehi A, Decomps P, Ben Gadri R, Ségur P and Mayoux C 1998 *J. Appl. Phys.* **83** 2950–7
[2] Massines F, Ségur P, Gherardi N, Khamphan C and Ricard A 2003 *Surf. Coat. Technol.* **174–175** 8–14
[3] Okazaki S, Kogoma M, Uehara M and Kimura Y 1993 *J. Phys. D: Appl. Phys.* **26** 889–92
[4] Yokoyama T, Kogoma M, Moriwaki T and Okazaki S 1990 *J. Phys. D: Appl. Phys.* **23** 1125–8
[5] Trunec D, Brablec A and Buchte J 2001 *J. Phys. D: Appl. Phys.* **34** 1697–9
[6] Roth J R, Tsai P P, Wadsworth L, Liu C and Spence P D 1995 *US Patent* #5,403,453
[7] Roth J R, Tsai P P, Liu C, Laroussi M and Spence P D 1995 *US Patent* #5,414,324
[8] Kelly-Wintenberg K, Hodge A, Montie T C, Deleanu L, Sherman D, Roth J R, Tsai P P and Wadsworth L 1999 *J. Vac. Sci. Technol.* **17** 1539–44
[9] Park J, Henins I, Herrmann H W and Selwyn G S 2001 *J. Appl. Phys.* **89** 15–19
[10] Park J, Henins I, Herrmann H W and Selwyn G S 2001 *J. Appl. Phys.* **89** 20–8
[11] Stark R H and Schoenbach K H 1999 *J. Appl. Phys.* **85** 2075–80
[12] Stark R H and Schoenbach K H 1999 *Appl. Phys. Lett.* **74** 3770–2

[13] Penache C, Bräuning-Demian A, Spielberger L and
     Schmidt-Böcking H 2000 *Proc. 7th Int. Symp. on High
     Pressure Low Temperature Plasma Chemistry
     (HAKONE VII) (Greifswald)* pp 501–5
[14] Eden J G *et al* 2003 *J. Phys. D: Appl. Phys.* **36**
     2869–77
[15] Park S-J, Wagner C J, Herring C M and Eden J G 2000
     Appl. Phys. Lett. **77** 199–201
[16] Geßner C, Scheffler P and Gericke K-H 2000 *Proc. 7th Int.
     Symp. on High Pressure Low Temperature Plasma
     Chemistry (HAKONE VII) (Greifswald)*
     pp 112–16
[17] Geßner C, Scheffler P and Gericke K-H 2001 *Proc. Int. Conf.
     on Phenomena in Ionized Gases (XXV ICPIG) (Nagoya)*
     vol 4, pp 151–2
[18] Schlemm H and Roth D 2001 *Surf. Coat. Technol.*
     142–144 272–6
[19] Gericke K-H, Geßner C and Scheffler P 2002 *Vacuum* **65**
     291–7
[20] Baars-Hibbe L, Sichler P, Schrader C, Geßner C,
     Gericke K-H and Büttgenbach S 2003 *Surf. Coat. Technol.*
     174–175 519–23
[21] Korzec D, Finantu-Dinu E G, Dinu G L, Engemann J,
     Stefecka M and Kando M 2003 *Surf. Coat. Technol.*
     174–175 503–8
[22] Baars-Hibbe L, Schrader C, Sichler P, Cordes T, Gericke K-H,
     Büttgenbach S and Draeger S 2004 *Vacuum* **73** 327–32
[23] Baars-Hibbe L, Sichler P, Schrader C, Gericke K-H and
     Büttgenbach S 2004 *Plasma Process. Polym.*
     at press
[24] Rai-Choudhury P 1997 *Handbook of Microlithography,
     Micromachining, and Microfabrication, vol 1:
     Microlithography* (Bellingham: SPIE Optical Engineering
     Press)
[25] O'Brien J, Hughes P J, Brunet M, O'Neill B, Alderman J,
     Lane B, O'Riordan A and O'Driscoll C 2001 *J. Micromech.
     Microeng.* **11** 353–8
[26] Roth J R 1995 *Industrial Plasma Engineering* (Bristol:
     IOP Publishing) pp 285, 418–19
[27] Wiesemann K 1976 *Einführung in die Gaselektronik*
     (Stuttgart: BG Teubner) pp 267–8
[28] Raizer Yu P 1997 *Gas Discharge Physics* (Berlin: Springer)
     pp 56, 133–5
[29] Grill A 1994 *Cold Plasma in Materials Fabrication*
     (New York: IEEE Press) pp 24–34
[30] Hartherz P 2002 *Dissertation* Darmstadt,
     ISBN 3-8322-0413-X
[31] Brown S C 1966 *Basic Data of Plasma Physics* (Cambridge:
     MIT Press) pp 219–35
[32] Schrader C, Sichler P, Baars-Hibbe L, Gericke K-H,
     Büttgenbach S and Draeger S 2004 at press
[33] Huxley L G H and Crompton R W 1974 *The Diffusion and
     Drift of Electrons in Gases* (New York: Wiley) pp 627–31
[34] Janzen G 1992 *Plasmatechnik* (Heidelberg: Hüthig) pp 40–3
[35] Sichler P, Büttgenbach S, Baars-Hibbe L, Schrader C and
     Gericke K-H 2004 *Chemical Eng. J. Special Issue 7th Int.
     Conf. on Microreaction Technology* vol 101 pp 465–8
[36] Scheffler P, Geßner C and Gericke K-H 2000 *Proc. 7th Int.
     Symp. on High Pressure Low Temperature Plasma
     Chemistry (HAKONE VII) (Greifswald)*, pp 407–11